

A THREE-DIMENSIONAL MODEL OF BERING AND CHUKCHI SEA

by
Shiao-Kung Liu* and Jan J. Leendertse*

Introduction

A part of the continental shelf area of the Bering and Chukchi Sea are now being opened up for oil exploration. For engineering and ecological risk analyses, extensive field data collection efforts are being carried out by various United States agencies and petroleum corporations to understand the hydrodynamic behavior of this vast offshore area.

In addition, modeling studies are being made for which a three-dimensional model of the area, outlined in Fig. 1, has been developed. This model is dynamically coupled to a two-dimensional stochastic weather model. This weather model contains a Markov synoptic component and a storm track component. The parameters of this model are derived from a 20-year data base.

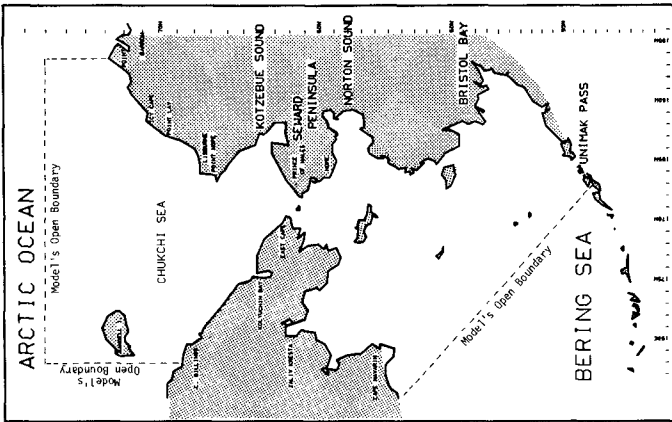
This paper presents a description of the three-dimensional model and the results of a series of simulations using the model to compute tidal propagation and circulations induced by tides and wind. The results of a simulation of a moving storm through the eastern Bering Sea are also presented.

The Three-Dimensional Modeling System

The modeling system used for the study is formulated according to the equations of motion for water and ice, continuity, state, the balance of heat, salt, pollutant and turbulent energy densities, on a three-dimensional finite difference grid. The vertical momentum, mass, heat and turbulent energy exchange coefficients are computed from the turbulent energy, thus the model contains a turbulence closure computation. Turbulent energy dissipation due to mixing of heavier water with lighter water is accounted for in the turbulence closure.

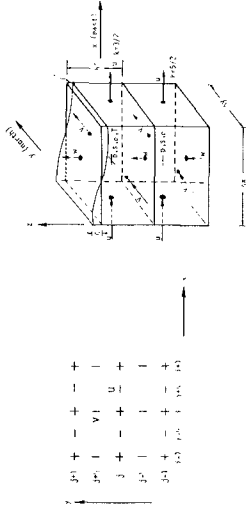
The horizontal grid conforms with the earth's ellipsoidal coordinates while the arbitrary vertical grid spacing approximates the bottom topography of the modeled area. The results are subsequently transformed on the Universal Mercator projection for graphical representation. For simplicity, the system of modeling equations is presented here by use of the standard finite difference notation on a regular spatial grid network in the horizontal direction, and on an irregular grid in the vertical (Fig. 2). The coordinates i, j, k, n , are used to denote discrete points on the x, y, z, t , domain. The finite difference formulation adapted for the computation takes the following form:

* The Rand Corporation, Santa Monica, California

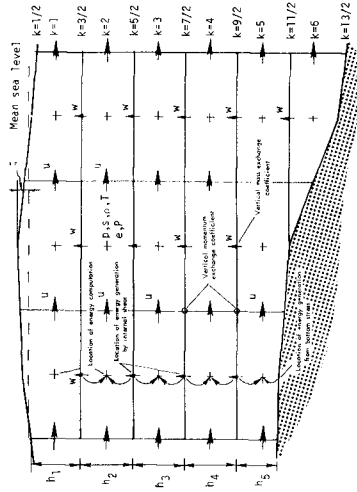


Location map showing eastern Bering Sea and Chukchi Sea modeling area.

Fig. 1



Space-staggered computation grid and relative position of variables



Location of variables on the xz plane

Fig. 2

$$\overline{\delta_t \zeta} = - \sum_k \left[\delta_x (\overline{h^x u}) + \delta_y (\overline{h^y v}) \right] \quad \text{at } i, j, n \quad (1)$$

where the variation of the water level ζ is derived from the continuity equation by vertical integration, and h is the layer thickness.

The momentum equation in the x-direction

$$\begin{aligned} \overline{\delta_t (h^x u)} = & - \delta_x (\overline{h^x u u^x}) - \delta_y (\overline{h^y v u^y}) - \overline{h^x} \delta_z (\overline{u^z w^x}) + f \overline{h^x v^x y} - \frac{1}{\rho^x} \overline{h^x} \delta_x p \\ & + \frac{1}{\rho^x} \left[h \delta_z (E_x \delta_z^{-2t}) + \delta_x (h A_x \delta_x u) + \delta_y (\overline{h^x A_y^x} \delta_y u) \right] \end{aligned} \quad (2)$$

at $i + \frac{1}{2}, j, k, n$

where E_x is the vertical momentum exchange coefficient, and A_x, A_y are horizontal exchange coefficients in x-direction and y-direction, respectively.

The momentum equation in the y-direction,

$$\begin{aligned} \overline{\delta_t (h^y v)} = & - \delta_x (\overline{h^x u v^x}) - \delta_y (\overline{h^y v v^y}) - \overline{h^y} \delta_z (\overline{v^z w^y}) - f \overline{h^y u^x y} - \frac{1}{\rho^y} \overline{h^y} \delta_y p \\ & + \frac{1}{\rho^y} \left[h \delta_z (E_y \delta_z^{-2t}) + \delta_x (\overline{h^y A_x^x} \delta_x v) + \delta_y (h A_y \delta_y v) \right] \end{aligned} \quad (3)$$

at $i, j + \frac{1}{2}, k, n$

The mass-balance equation for salt,

$$\begin{aligned} \overline{\delta_t (hs)} = & - \delta_x (\overline{h^x u s^x}) - \delta_y (\overline{h^y v s^y}) - h \delta_z (\overline{w s^z}) \\ & + \delta_x (\overline{h^x D_x \delta_x s}) + \delta_y (\overline{h^y D_y \delta_y s}) - h \delta_z (\kappa \delta_z^{-2t}) \end{aligned} \quad (4)$$

at i, j, k, n

where D_x and D_y are the horizontal diffusion coefficients and κ is the vertical mass exchange coefficient. For temperature

$$\begin{aligned} \overline{\delta_t(hT)}^t &= -\delta_x(\overline{h^x u T^x}) - \delta_y(\overline{h^y v T^y}) - h\delta_z(\overline{w T^z}) \\ &+ \delta_x\left(\overline{h^x D_x \delta_x T}\right)_- + \delta_y\left(\overline{h^y D_y \delta_y T}\right)_- + h\delta_z\left(\overline{\kappa' \delta_z T^2 t}\right) \end{aligned} \quad (5)$$

at i, j, k, n

where κ' is the vertical thermodiffusion coefficient.

For the SGS energy density in the system,

$$\begin{aligned} \overline{\delta_t(he)}^t &= -\delta_x(\overline{h^x u e^x}) - \delta_y(\overline{h^y v e^y}) - h\delta_z(\overline{w e^z}) \\ &+ \delta_x\left(\overline{h^x D_x \delta_x e}\right)_- + \delta_y\left(\overline{h^y D_y \delta_y e}\right)_- + h\delta_z\left(\overline{E_e \delta_z e^{-2} t}\right) \\ &+ h\overline{\delta_e^z} - D_e h \end{aligned} \quad (6)$$

at i, j, k, n

where E_e is the vertical momentum exchange coefficient. For the pollutant constituent concentration,

$$\begin{aligned} \overline{\delta_t(hP)}^t &= -\delta_x(\overline{h^x u P^x}) - \delta_y(\overline{h^y v P^y}) - h\delta_z(\overline{w P^z}) \\ &+ \delta_x\left(\overline{h^x D_x \delta_x P}\right)_- + \delta_y\left(\overline{h^y D_y \delta_y P}\right)_- + h\delta_z\left(\overline{\kappa \delta_z P^2 t}\right) \\ &+ h\overline{\delta_P} - D_P h \end{aligned} \quad (7)$$

at i, j, k, n

The equation of state is approximated by

$$\begin{aligned} \rho &= \left[5890 + 38T - 0.375T^2 + 3s \right] / \left[\left(1779.5 + 11.25T - 0.0745T^2 \right) \right. \\ &\quad \left. - \left(3.8 + 0.01T \right) s + 0.698 \left(5890 + 38T - 0.375T^2 + 3s \right) \right] \end{aligned} \quad (8)$$

at $i, j, k, n + 1$

The continuity equation is used to compute the vertical velocity:

$$\delta_z w = -\delta_x(\overline{h^x u}) - \delta_y(\overline{h^y v}) \quad \text{at } i, j, k, n + 1 \quad (9)$$

Similar equations for velocity components u and v can be written for the top and bottom layers, but now the effects of wind and bottom friction must be considered. We have at the surface:

$$\begin{aligned} \overline{\delta_t(\overline{h^x u})}^t &= -\delta_x(\overline{h^x u u^x}) - \delta_y(\overline{h^y v u^y}) - \overline{h^x} \delta_z(\overline{u^z w^x}) + f \overline{h^x v^x y} - \frac{1}{\rho^x} \overline{h^x} \delta_x p \\ &+ \frac{1}{\rho^x} \left[\theta \rho_a w_a^2 \sin \psi - \left(E_x \delta_z \overline{u^2 t} \right)_{k=3/2} + \delta_x (h A_x \delta_x u)_- + \delta_y \left(\overline{h^x A_y^x y} \delta_y u \right)_- \right] \end{aligned}$$

at $i + \frac{1}{2}, j, 1, n$ (10)

where ψ is the clockwise angle between the model's y -axis and the direction toward which the wind is blowing. In the y -direction, the momentum equation becomes

$$\begin{aligned} \overline{\delta_t(\overline{h^y v})}^t &= -\delta_x(\overline{h^x y v^x}) - \delta_y(\overline{h^y v v^y}) - \overline{h^y} \delta_z(\overline{v^z w^y}) - f \overline{h^y u^x y} - \frac{1}{\rho^y} \overline{h^y} \delta_y p \\ &+ \frac{1}{\rho^y} \left[\theta \rho_a w_a^2 \cos \psi - \left(E_y \delta_z \overline{v^2 t} \right)_{k=3/2} + \delta_x \left(\overline{h^y A_x^y x} \delta_x v \right)_- + \delta_y \left(h A_y \delta_y v \right)_- \right] \end{aligned}$$

at $i, j + \frac{1}{2}, 1, n$ (11)

where θ represents the wind-stress coefficient, w_a is wind speed, and ρ_a represents the density of air. At the bottom layer, the momentum equation becomes

$$\begin{aligned} \overline{\delta_t(\overline{h^x u})}^t &= -\delta_x(\overline{h^x u u^x}) - \delta_y(\overline{h^y v u^y}) - \overline{h^x} \delta_z(\overline{u^z w^x}) + f \overline{h^x v^x y} - \frac{1}{\rho^x} \overline{h^x} \delta_x p \\ &+ \frac{1}{\rho^x} \left\{ \left(E_x \delta_z \overline{u^2 t} \right)_{k=K-\frac{1}{2}} - \rho^x g u_- \left[u_-^2 + \left(\frac{\overline{xy}}{v_-} \right)^2 \right]^{\frac{1}{2}} / \left(\overline{C^x} \right)^2 \right. \\ &\left. + \delta_x \left(h A_x \delta_x u \right)_- + \delta_y \left(\overline{h^x A_y^x y} \delta_y u \right)_- \right\} \end{aligned}$$

at $i + \frac{1}{2}, j, K, n$ (12)

$$\begin{aligned} \overline{\delta_t(\overline{h^y v})} &= -\delta_x(\overline{h^x u v^x}) - \delta_y(\overline{h^y v v^y}) - \overline{h^y} \delta_z(\overline{v^z w^y}) - \overline{f h^y u^{xy}} - \frac{1}{\rho_y} \overline{h^y} \delta_y p \\ &+ \frac{1}{\rho_x} \left\{ \left(E_y \delta_z \overline{v^2 t} \right)_{k=K-\frac{1}{2}} - \overline{\rho^y} g v_- \left[\left(\overline{u^{xy}} \right)^2 + v_-^2 \right]^{\frac{1}{2}} \right\} / \left(\overline{C^y} \right)^2 \\ &+ \delta_x \left(\overline{h^y A_x^x} \delta_x v \right)_- + \delta_y \left(\overline{h A_y} \delta_y v \right)_- \quad \text{at } i, j + \frac{1}{2}, K, n \quad (13) \end{aligned}$$

where C is Chezy coefficient.

In the modeled area, each vertical motion of water mass has to work against buoyancy forces induced by the density gradient. If the available kinetic energy of the turbulent motion is insufficient to overcome this stabilizing effect, turbulence is inhibited and suppressed. As a consequence, the process of momentum and mass-heat exchange will be lower than the neutral stability condition. The criteria for the onset of this turbulence-suppressing process in the system can be obtained by the local density gradient and turbulent energy level. Therefore, the variability of the vertical exchange coefficients in the model is computed by a turbulence closure technique using local turbulence intensity e.

$$E_y = \overline{\rho^y z} \overline{L \sqrt{e}^{-xz}} \quad (14) \quad E_x = \overline{\rho^{xz}} \overline{L \sqrt{e}^{-xz}} \quad (15)$$

$$E_e = a_1 \overline{L \sqrt{e}^{-z}} \quad (16) \quad \kappa = a_4 \overline{L \sqrt{e}^{-z}} \quad (17)$$

where a_1, a_4 are turbulence closure constants and L denotes the length scale, which can be approximated by an additional transport equation or by a parametric expression such as

$$L = \kappa' z (1 - z/d)^{\frac{1}{2}} \quad (18)$$

κ' is the von Karman constant, z represents the vertical distance from the bottom to the point considered, and d is the vertical distance from the surface to the bottom.

In the horizontal direction, the exchange coefficient is computed in two parts as a function of the local vorticity gradient and the local grid dimension. The first part is

$$A = \gamma |(\delta_x \bar{\omega}^y + \delta_y \bar{\omega}^x)| (\Delta l)^3 \quad (19)$$

where ω is the vorticity, γ is a coefficient, and Δl is the local grid size. This part represents the exchange for a wave number lower than the spatial Nyquist frequency. The second part represents the contribution from the homogeneous subgrid scale turbulence above the spatial Nyquist frequency, which can be computed according to Kolmogorov's turbulence spectrum theory. The gross horizontal exchange coefficient is therefore

$$D_x = \bar{A}^x + a_5 \Delta l^{4/3} \quad D_y = \bar{A}^y + a_5 \Delta l^{4/3} \quad (20) \quad (21)$$

where a_5 is a function of the energy dissipation rate. In the model, the amount of reduction in the vertical exchange due to stratification is based on the direct computation of the local gain in potential energy induced by vertical mixing. The exact amount is then taken out of the local turbulent (kinetic) energy budget. In the equation of energy (Eq. 6), the generation and dissipation terms become

$$\begin{aligned} \bar{S}_e^z - D_e &= a_3 \underbrace{\overline{L\sqrt{e}^z} \left[(\delta_z \bar{u}^x)^2 + (\delta_z \bar{v}^y)^2 \right]}_{(1)} + a_3 \underbrace{\overline{L\sqrt{e}^z} \frac{g}{h^z \rho} (\delta_z \bar{\rho}^z)}_{(2)} \\ &\quad - \underbrace{a_2 e^{3/2}/L}_{(3)} \end{aligned} \quad (22)$$

where the first term denotes production, the second term represents the portion supplied that is used in potential energy increase, and the third term is dissipation.

Modeling of Tides and Currents

Tide enters the Bering Sea through the central and western Aleutian, and enters the Chukchi Sea from the East Siberian Sea. The largest tidal amplitudes are found over the Bering shelf region and in these regions substantial tidal velocities can be observed. The tidal velocities in the Chukchi Sea are much smaller except in areas north of the Bering Strait where two tidal systems interact.

To study the tidal dynamics of the coastal system, the deep water tides at the model's open boundaries are generated using astronomical tidal prediction coefficients obtained from field measurements. A period in the beginning of August 1976 was selected for simulation as current data was available for this period which could be used for comparison of model results with field data. The simulations indicated that the propagation of tide in the study area is dominated by the bathymetry (Fig. 3), and to a certain extent, also influenced by the vertical density structure. The latter was known to cause the shifting of the location of amphidromic points during summer when strong pycnocline exist. Figure 4 shows an instantaneous distribution of computed tidal currents and water level in the modeled area projected on the Mercator plotting scale. As the figure indicates, at 0600 hours (GMT) on August 2, 1976, ebb tide occurred over the shelf break in the eastern Bering Sea. At the same time, water levels were rising in the Bristol Bay, Norton Sound, and over most of the Chukchi Sea.

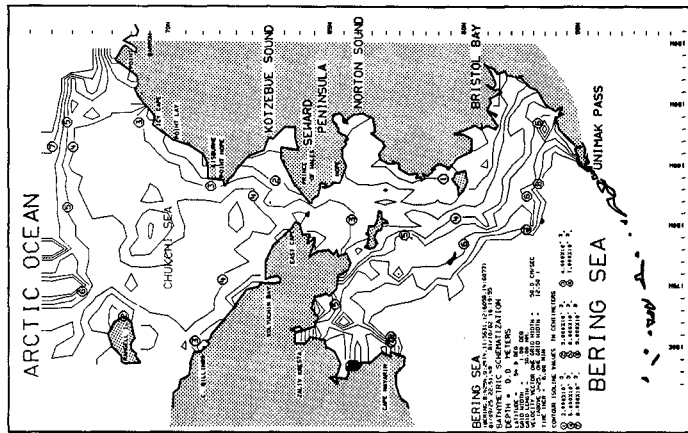
To represent the tidal propagation in an efficient way co-tidal and co-range charts were prepared. The computed co-tidal chart for the semi-diurnal tidal component (Fig. 5) indicates that there are six major amphidromic systems in the modeled area. Over the eastern shelf area, the computed amplitude and phase, as well as the locations of the amphidromic points, agree extremely well with the observed values (Fig. 6) compiled by the National Oceanic and Atmospheric Administration. The computed co-tidal chart for the diurnal tidal components (Fig. 7) also agrees extremely well with the chart derived using observed data (Fig. 8).

Tidal currents in the study area have also been compared to the field data. Using a more detailed sub-model of the Bristol Bay, the computed tidal currents agree extremely well to the observed current data (Figs. 9, 10).

Tide-induced and Baroclinic Circulation

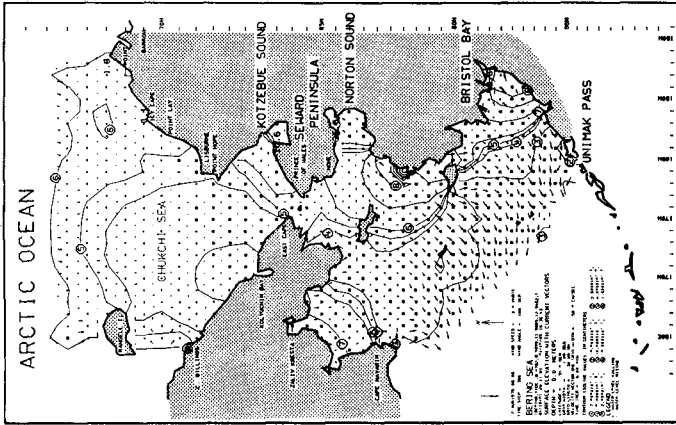
Circulation and transport associated with tidal propagation constitute one of the most important and everlasting driving mechanisms in coastal waters. The non-linear mechanisms generate net circulation over the shallow water in addition to the tidal excursion. This net "residual" transport is usually responsible for carrying constituents to areas much beyond the extent of tidal excursion over the time span of weeks or months. Therefore, one of the major functions of the three-dimensional model has been the determination of the tidal residual circulations.

When a long wave (e.g., the tide) propagates from the deep water through the shallow areas, the non-linear advection terms in the equation of motion, along with non-linear transport terms, generate higher harmonics of the fundamental frequency. In particular, the second harmonic increases in amplitude with the distance of propagation. Bottom friction generates odd harmonics. The varying depth and complicated boundaries



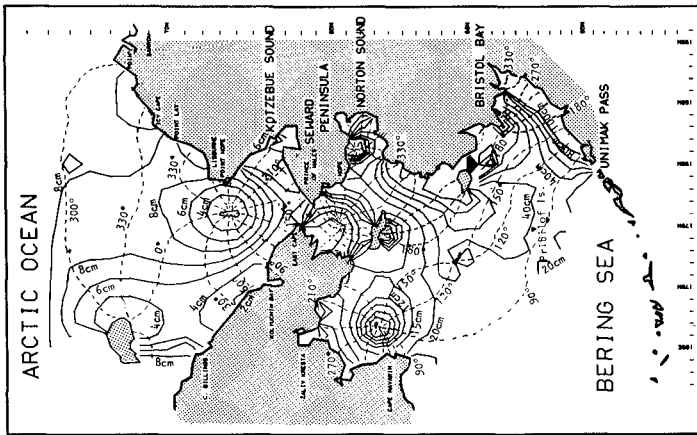
Bathymetric schematization of the three-dimensional model of Bering and Chukchi Sea.

Fig. 3



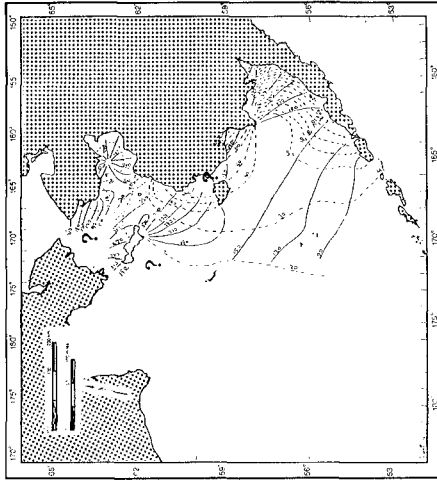
Computed tidal currents and water level distributions in the Bering/Chukchi Sea. Water level rise while a square (□) indicates falling of local water surface.

Fig. 4



Compiled tidal chart for the semidiurnal tidal component using the three-dimensional model of Bering/Chukchi Sea.

Fig. 5



Co-tidal chart for the semidiurnal tidal component H_2 compiled by NOAA according to existing data.

Fig. 6

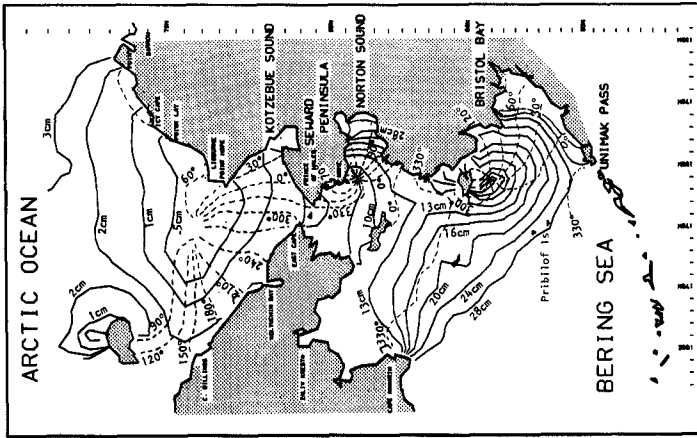
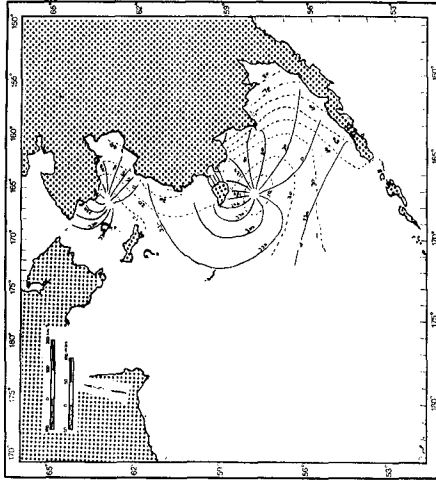


Fig. 7 Computed co-tidal chart for the diurnal tidal component using the three-dimensional model of Bering/Chukchi Sea.



Co-tidal chart for the diurnal tidal component (M) compiled by NOAA according to existing data.

Fig. 8

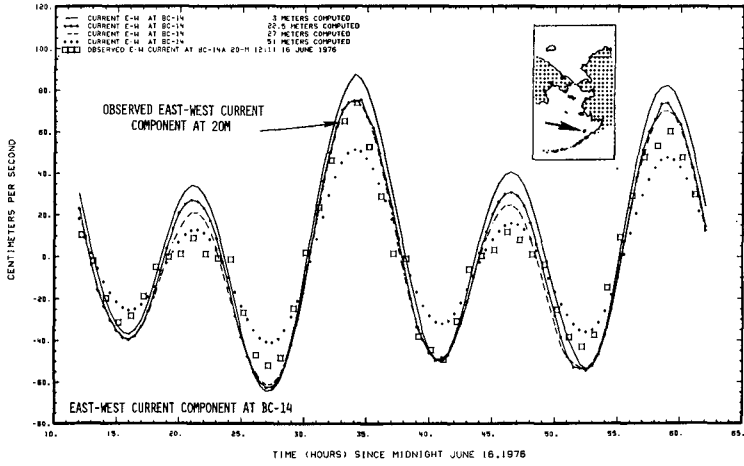


Fig. 9 Observed east-west current component at station BC-14 and the computed values at the nearby gridpoint

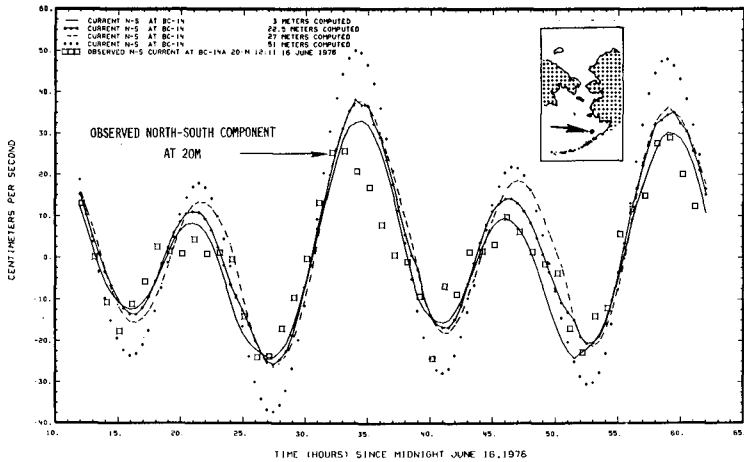


Fig. 10 Observed north-south current component at station BC-14 and the computed values at the nearby gridpoint

generate dispersion of energy by a combined effect described above and by the generation of local circulation through advection. Due to the non-homogeneity of the density in the vertical, the velocities over any vertical are generally not uniform in magnitude and direction. Since advection is the main mechanism by which the tidal residual is generated, a three-dimensional model is required to compute this non-linear circulation at various levels in the water column. The tidal residual circulation pattern is extremely difficult to establish by measurement as only a limited number of current meters can be employed in these vast areas. In addition, these residual currents are difficult to measure accurately because its magnitude is usually below the sensitivity of most current meters. Even with drogues, the wind effects are difficult to separate from the tidal residual components.

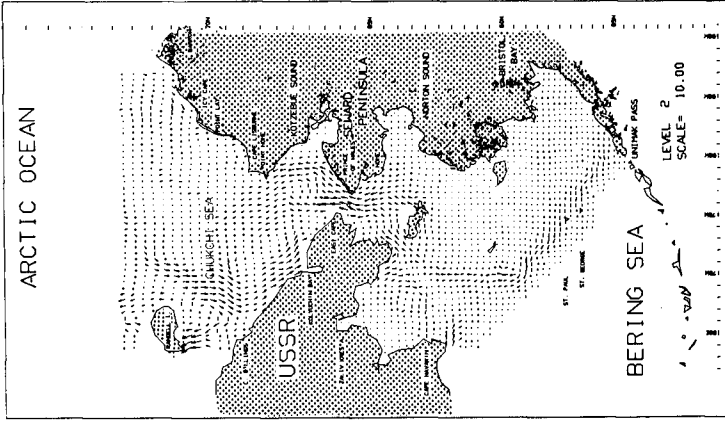
The seasonal changes of the density field in the horizontal direction contributes also to the residual circulation through the mechanisms in the baroclinic modes. Consequently, the residual circulation of a coastal area should be studied by considering both barotropic (tides, etc.) and baroclinic modes. In most cases, residual circulations derived from models using field data for adjustments, is extremely difficult to separate the contributions from these two different modes.

Field data collected over the past decades seems to indicate that the residual transport is from the Pacific Ocean to the Arctic Ocean through the Bering Strait. However, because of the vast area involved, it is rather difficult to obtain a set of records free from the weather's (wind) influence on the residual transport. In order to determine the net circulation pattern, simulations were made using the model with only tides and density field as its inputs. The computed tidal ellipses and residual circulation pattern in the surface layer for the summer season are shown in Figs. 12 and 13. It is derived by a numerical filtering process using a tidal eliminator. Again, the residual transport contains contributions both from tide and from the density field. One of the significant features is the northward transport along the shelf break (depth = 300 m) and along the 50-m isobath. Along this isobath is a transition from a well-mixed system in the shallower area to a two layer system. The general direction of the transport at this transition agrees with the basic theory of coastal residual circulations of non-homogeneous waters. It also agrees with the general drift of satellite-tracked drogues released in various locations in the Bering Sea.

Residual transport through the Bering Strait have been the subject of significant interest in the oceanography of the Pacific Ocean and the Arctic Ocean. The computed residual transport through the Bering Strait is about 0.5 Sv. in the absence of the north-south atmospheric gradient. This agrees with the value observed by Tripp, et al (Ref 1). Another large scale field monitoring program is presently being conducted to further confirm this.

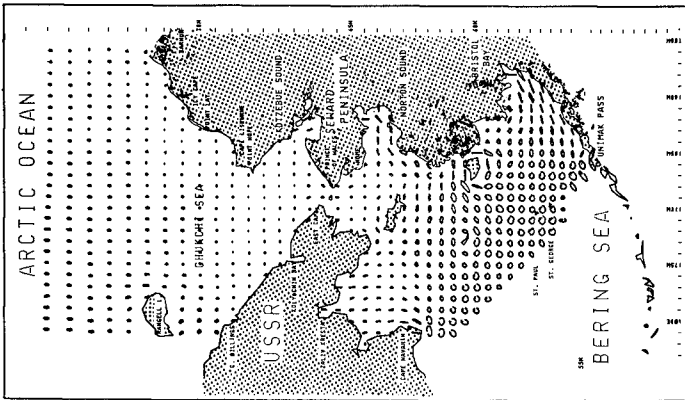
Figure 14 shows the components of the tidal velocities at six different depths of a station in the Bering Strait. The east-west component of the velocities are predominately eastward and only during a short period in the tidal cycle the flow reverses.

The north-south components of the velocities are nearly always directed toward the north. The maximum velocity is in the surface layer and is 22 cm/sec. The magnitude of the current at that time is about 23 cm/sec and the direction is about 17° from the North. Higher modes (overtides)



Computed residual current in the second layer using a plotting scale of 10 cm/sec per horizontal grid-spacing

Fig. 12



Computed 12.5-hour tidal ellipses in the second layer using a plotting scale of 86 cm/sec per horizontal grid-spacing

Fig. 11

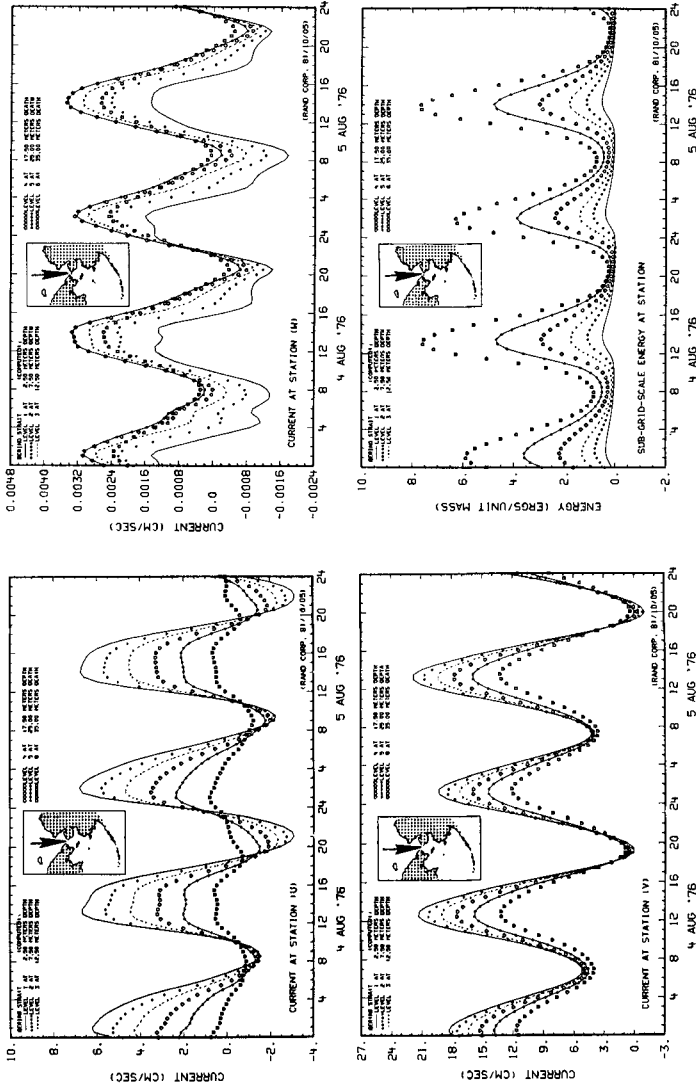


Fig. 13 Computed tidal velocities ($U = E-W$, $V = N-S$ components) in six representative layers at a station in the Bering Strait.

Fig. 14 Computed vertical velocity (W) and the turbulent energy intensities in six representative layers at a station in the Bering Strait.

can be noticed in the computed currents. They appear mainly in the lower layers where frictional effects are strong and the velocities lag behind those in the upper layers. These characteristics are more obvious in the computed vertical velocity components (top graph, Fig. 14).

The turbulence variation in the bottom layer leads the variation on the upper layers as the transfer is inefficient by the vertical pycnostructure as shown in the bottom graph of Fig. 14. Note that the greatest turbulence intensity exist in the bottom layer. The intensities in this layer are indicated by small squares.

The vertical variation of velocities, energy densities and their phase differences are due mainly to the density variation (Fig. 15). The depth of thermocline in this area are generally deeper than the pycnocline associated with the salinity. This may be due to the more efficient heat diffusion process than the vertical mass exchange.

Residual circulation and stratification-related turbulence field also influence the diffusion process. The amount of diffusion and the net displacement varies throughout a water column. As illustrated in Fig. 16, for a case without surface wind stress particle group releases in the top layer experiences different amounts of advection, turbulent diffusion and net transport than the group release in a lower layer over a 24-hour period.

Storm-Induced Responses

The modeled area is situated within the climatological zone of "Aleutian Lows" which is one of the two major storm areas in the northern hemisphere (the other, Icelandic Lows). The average occurrence of a storm is approximately 3.5 per month with an average duration of 1.5 days.

Many simulations with a moving storm have been made. The weather inputs were derived from a simulation of the weather model. A typical wind and pressure field generated by the stochastic weather model (Ref. 2) is shown in Fig. 17. This particular storm is moving with a speed of 5.1 m/sec.

The computed flow field in the surface layer of the three-dimensional model are shown in Fig. 18, together with the contour lines of the water levels.

At the time of the graph a storm setup occurs in Bristol Bay and in the area northeast of Cape Navarin while low water levels are present in Norton Sound.

Model Use

The three-dimensional model and the stochastic weather are used together with a wind variability model to make simulations of the movements of spilled oil in case accidents would occur during oil exploration or exploitation. The movements are simulated for periods of one to two months originating from selected hypothetical spill sites. The movements can be traced either on the water surface, in or under the ice cover or dispersed in the water column

Results of many simulations are subsequently used to define the risk that certain sensitive areas are exposed to accidentally discharged oil.

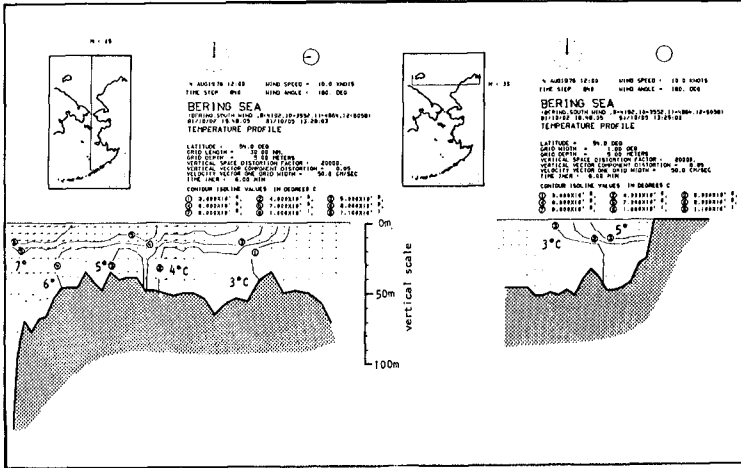


Fig. 15 Vertical temperature distributions through two cross-sections of the model.

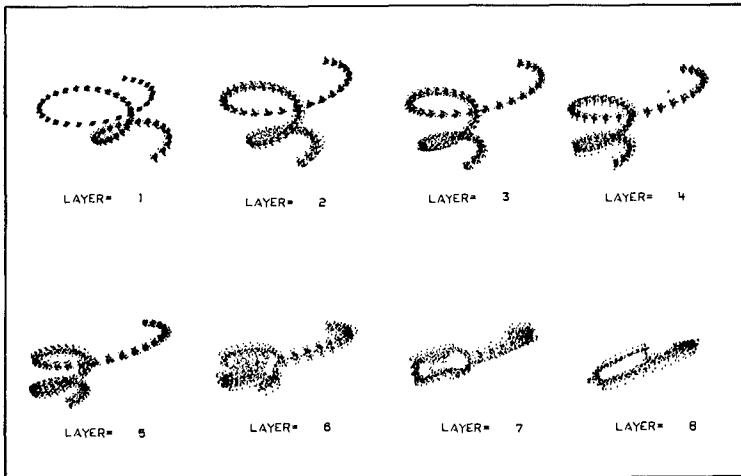
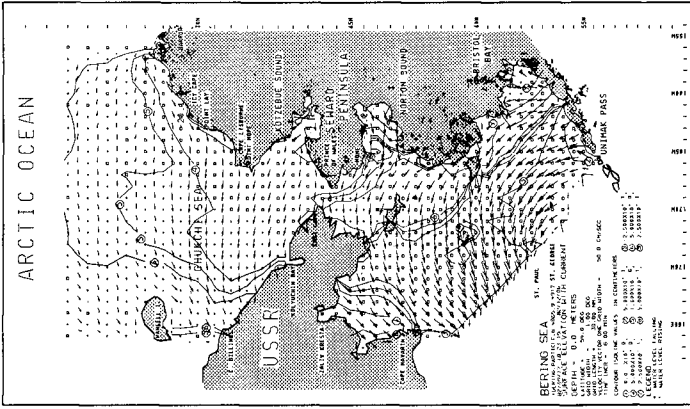
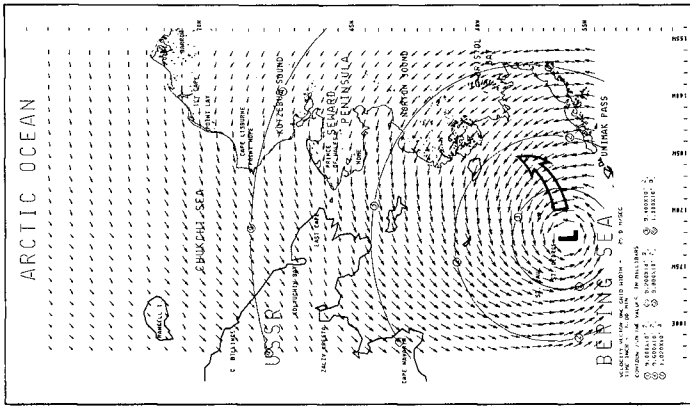


Fig. 16 Partially insulated by the pycnocline, 24-hour trajectories of particle groups released in the upper five layers experience less turbulent diffusion than the lower layers when the system is forced only with tidal energies



Water surface elevation and surface current distribution induced by the moving low pressure center shown in Fig. 17.

Fig. 18



Synoptic wind field as generated by a moving low pressure system. The maximum 10-meter wind speed is approximately 30 meters per second.

Fig. 17

ACKNOWLEDGMENTS

This study was supported by the U.S. Bureau of Land Management through interagency agreement with the National Oceanic and Atmospheric Administration (NOAA), under which a multi-year program responding to needs of petroleum development of the Alaskan Continental Shelf is managed by the Outer Continental Shelf Environmental Assessment Program (OCSEAP) Office.

The authors would like to express their appreciation to Drs. R. Overstreet, M. Pelto, J. Schumacher, H. Mofjeld, C. Pearson, C. Pease, J. Overland, M. Reynolds, and G. Hufford (all from NOAA); S. Martin, K. Aagaard, and R. Tripp (from the University of Washington); W. Stringer and G. Weller (from the University of Alaska); D. Amstutz, R. Emerson, and B. Morris (from the Bureau of Land Management); and K. Lanfer, W. Samuels, and Robert LaBelle (from the U.S. Geological Survey) for providing data and valuable discussion during the course of our investigation. The authors obtained much support from the Technical Project Officer, M. Pelto, in arranging the field data survey for the model study and in coordinating their work with the efforts of other study groups.

Thanks also go to our Rand colleagues, A. B. Nelson and Ms. C. Johnson who modified various graphical programs for displaying simulation results on the Mercator projection and G. Coughlan for her efforts in paper preparation.

REFERENCES

1. Tripp, R. B., L. K. Coachman, K. Aagaard and J. D. Schumacher, *Low Frequency Components of Flow in the Bering Strait System*, American Geophysical Union Meeting, pp. 0-4, September 1978.
2. Liu, S. K., *Stochastic Analyses and Control of Estuarine-Coastal Water Quality Systems: Vol. II. A Stochastic Weather Model for Oil-Spill Analysis*. The Rand Corporation, (in preparation).